View metadata, citation and similar papers at core.ac.uk
brought to you by CORE
provided by NASA Technical Reports Server

Optical Properties of Tm^{3+} ions in Alkali Germanate Glass

Brian M. Walsh, Norman P. Barnes, Donald J. Reichle
NASA Langley Research Center, Hampton, VA 23681

Shibin Jiang
NP Photonics, Tucson, AZ 85747

Abstract: Tm-doped alkali germanate glass is investigated for use as a laser material. Spectroscopic investigations of bulk Tm-doped germanate glass are reported for the absorption, emission and luminescence decay. Tm:germanate shows promise as a fiber laser when pumped with 0.792 μm diodes because of low phonon energies. Spectroscopic analysis indicates low nonradiative quenching and pulsed laser performance studies confirm this prediction by showing a quantum efficiency of 1.69.

OCIS codes: (140.3580) Lasers, solid state, (140.3510) Lasers, fiber, (140.3480 Lasers, diode pumped

1. Introduction

One approach to Tm lasers uses materials co-doped with Yb and Er and ≈0.95 μm pump diodes. With this approach, Yb absorbs the pump photons, transfers the energy to Er, which subsequently transfers the energy to the Tm upper laser manifold. Even in the ideal case where every energy transfer process has unity efficiency, the ratio of photon energies limits the efficiency to ≈0.5. Another approach pumps Tm directly in the $^3H_4$ manifold at 0.79 μm. If each pump photon produces only 1 Tm atom in the upper laser manifold, the $^3F_4$, then the ratio of pump to laser photon energies limits the efficiency to ≈0.4. However, Tm pumped by a 0.79 μm diode laser undergoes self-quenching. This produces two Tm atoms in the upper laser manifold. In this situation, the quantum efficiency is ideally 2.0 and the efficiency limit increases to ≈0.8. In Tm doped laser materials nonradiative decay competes with self-quenching. In silica glass, nonradiative decay is very competitive because the phonon energies of silica are high, extending to 1100 cm^{-1} [1]. Thus, the quantum efficiency is near 1.0 rather than 2.0. Germanate glass does not suffer as severely from this problem because the phonon energies are lower, extending to only 900 cm^{-1} [2]. In lanthanide doped glasses and crystals the highest energy phonons exercise the most influence in nonradiative relaxations because multiphonon decay occurs with the fewest number of phonons required to bridge the energy gap between two manifolds. To combat the deleterious effects of nonradiative decay, Tm:germanate glass is investigated. There are very few studies of the optical properties of Tm in germanate glass [3-13], and those in recent years concentrate on lead germanates [8-10, 12,13]. This study concentrates on alkali germinates.

One of the important reasons that we use alkali germanate glasses is that such a glass can be processed in a platinum crucible safely. Lead germanate glass could lead to damage of the platinum crucible, especially under inert atmosphere environment.

2. Experimental Method

The alkali germanate glasses studied here are composed of, in mol%, GeO_2(50-70%), Na_2O/Li_2O(5-20%), BaO/CaO(5-20%), Al_2O_3(2-15%), La_2O_3(0.5-6%). The exact percentages for the sample compositions studied here are not known since the samples were obtained from a commercial company, NP Photonics, and the exact composition is proprietary. The samples were doped with 2 and 4 mol% Tm_2O_3, which replaces La_2O_3 substitutionally.

High purity chemicals with less than 5 ppm of iron and copper are used as the starting materials. Glass melting are processed in platinum crucibles. The hydroxyl ion OH- concentration in these glasses are removed by bubbling the glass with nitrogen gas. A low OH^- content is important in order to eliminate the non-radiative energy transfer from the excited level of Tm^{3+} ion to OH^-. The glasses were cast into an aluminum mold and annealed in a furnace. A Rod-in-Tube fiber drawing technique was used for fiber fabrication. The core glass rod was drilled from a bulk glass, and the barrel of the rod will be polished to a high surface quality. Cladding glass tubes was drilled from a cladding glass. Both inside and outside surfaces of the glass tubes was polished to a high surface quality. The inside diameter of the inner cladding tube matched very well with the diameter of the core glass rod.

Key spectroscopic parameters include the lifetime, absorption and emission cross-section, as well as Judd-Ofelt parameters. They were measured using Tm:germanate materials with 2 different Tm concentrations. The density of the Tm atoms was calculated using the measured density and the quoted weight fraction of Tm. The material density was measured as 4.174 g/cm^3. For a given weight fraction, W, the Tm density, N_0, is calculated as $2W\rho/M_M$ where ρ is the density and M_M is the mass of a Tm_2O_3 molecule, 7.2035×10^{-22} g. The factor of 2 arises from having 2 Tm atoms per molecule. For the 0.02 Tm sample, the number density of Tm atoms is 2.62×10^{20} cm^{-3}.

The decay lifetime of the $^3H_4 \rightarrow {}^3H_6$ emission near 0.79 μm and the $^3F_4 \rightarrow {}^3H_6$ emission near 2.0 μm was measured by exciting Tm:germanate samples with a 1.8 μm pulsed Co:MgF_2 laser and pulse widths < 5 ns. A large number of traces were averaged on a digitizing oscilloscope.

Transmission spectra were measured between 0.3 and 2.1 μm on a Perkin-Elmer Lambda 900 spectrophotometer. The transmission data was corrected for Fresnel losses at the sample faces and used to obtain the absorption cross-section. Tm absorption for the $^1D_2$, $^1G_4$, $^3F_2 + {}^3F_3$, $^3H_4$, $^3H_5$, and $^3F_4$ manifolds are clearly identifiable. The results are shown in Figure 1. Using the error propagation method, we estimated that the absorption cross sections are accurate to approximately ± 5%. This is largely due to concentration uncertainty.

The emission cross-section of the $^3F_4 \rightarrow {}^3H_6$ transition was measured. A Tm:germanate emission spectrum from 1.5 to 2.2 μm was recorded under a diode laser excitation at 0.785 μm. Fluorescence of the Tm:germanate sample was corrected for the response of the monochromator and cooled InSb detector. Using the error propagation

method, we estimated that the emission cross sections are accurate to approximately ±18%.

A diode pumped Tm:germanate fiber laser was constructed and evaluated. A collimated 30 W peak power laser diode passed through a dichroic that was designed to be highly transmissive at the pump wavelength and simultaneously highly reflective at the laser wavelength. An antireflection coated, 20 mm focal length lens concentrated the pump radiation on the Tm:germanate fiber. The other end of the fiber was butt coupled to a plane, highly reflective mirror. The laser output energy was collimated by the same lens used to concentrate the pump light and then separated by the dichroic. An RG 1000 color glass filter rejected any scattered pump light. An energy meter with a 5.0 ms integration time, matching the pump pulse length, measured the pump energy and laser output energy. The pump energy was measured between the laser diode array and the dichroic. No correction for the transmission of the dichroic and lens was used.

Both laser output energy and transmitted pump energy were measured as a function of the pump energy. Transmitted pump energy was measured by removing the highly reflecting mirror and measuring the energy with and without the RG 1000 color glass filter. The energy obtained with the color glass filter, after correcting for the transmission, was subtracted from the total energy to represent the unabsorbed pump radiation. Wavelength was measured using a 0.5 m monochromator with a 600 g/mm grating and a cooled InAs detector.

3. Results

3.1 Spectroscopy

In observing the absorption of the $^3F_4$ manifold in Tm:germanate glass it is noticed that it exhibits a double peak structure which is not seen in Tm:silica or Tm:ZBLAN glasses[14]. This is partially true for the $^1G_4$ manifold as well, where it is somewhat evident for Tm:ZBLAN, but not for Tm:silica. This likely indicates a localized symmetry about the Tm ions in germanate glasses. The absorption cross sections measured look very similar to those measured by Wang [8] for Tm-doped lead germanate glass and have similar values for the cross section. They are also in fair agreement with those reported by Balda [13].

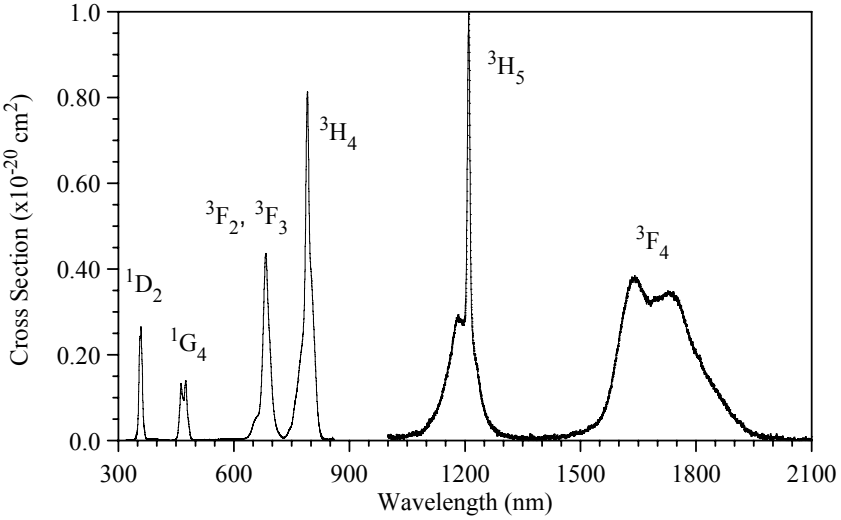

Fig. 1. Absorption cross section spectra of Tm:germanate glass.

The manifold, wavelength range, mean wavelength, $\bar{\lambda}$, mean energy, $\bar{E}$, and the integrated cross section, $\int \sigma(\lambda)d\lambda$, are collected in table 1. The values tabulated here will be useful for input values required for a Judd-Ofelt analysis.

Table 1. Absorption parameters of Tm:germanate glass.

Manifold	Range (nm)	$\bar{\lambda}$ (nm)	$\bar{E}$ (cm^{-1})	$\int \sigma(\lambda)d\lambda$ (cm^2-nm)
$^1D_2$	345-375	359	27847	$2.87x10^{-20} \pm 0.34$
$^1G_4$	440-495	470	21271	$2.82x10^{-20} \pm 0.34$
$^3F_2$, $^3F_3$	635-725	682	14659	$10.71x10^{-20} \pm 1.28$
$^3H_4$	725-825	789	12671	$19.69x10^{-20} \pm 2.36$
$^3H_5$	1025-1350	1192	8387	$34.84x10^{-20} \pm 4.18$
$^3F_4$	1450-2050	1708	5853	$86.91x10^{-20} \pm 9.42$

The Judd-Ofelt theory [15,16,17] allows for the calculation of manifold-to-manifold transition probabilities, from which the radiative lifetimes and branching ratios of emission can be determined. A Judd-Ofelt analysis relies on accurate absorption measurements, specifically the integrated absorption cross section over the wavelength range of a number of manifolds. From the integrated absorption cross section, the line strength, S_m, can be found

$$S_m = \frac{3ch(2J'+1)}{8\pi^3 e^2 \bar{\lambda}} n\left(\frac{3}{n^2+2}\right)^2 \int_{manifold} \sigma(\lambda)d\lambda \qquad (1)$$

where J' is the total angular momentum of the lower state, found from the $^{2S+1}L_J$ designation. The mean wavelength, $\bar{\lambda}$, is found by the first moment of the spectral data,

$\Sigma\ \lambda\sigma(\lambda)/\Sigma\ \sigma(\lambda)$, and the other symbols have their usual meaning. The utility of the Judd-Ofelt theory is that it provides a theoretical expression for the line strength, given by

$$S_{ED} = \sum_{t=2,4,6} \Omega_t \left| \left\langle f^n [SL] J \left\| U^{(t)} \right\| f^n [S'L'] J' \right\rangle \right|^2 \tag{2}$$

where Ω_t are the Judd-Ofelt parameters and the term in brackets are doubly reduced matrix elements in intermediate coupling. A Judd-Ofelt analysis minimizes the square of the difference between S_m and S_{ED}, with Ω_t as adjustable parameters. Following this procedure, the Judd-Ofelt parameters are found to be $\Omega_2 = 6.14\text{x}10^{-20}$, $\Omega_4 = 1.54\text{x}10^{-20}$ and $\Omega_6 = 0.873\text{x}10^{-20}$ cm^2. The electric dipole transition probability, A_{ED}, for any excited state transition can now be calculated

$$A_{ED} = \frac{64\pi^4 e^2}{3h(2J+1)\bar{\lambda}^3} \left[n \left(\frac{n^2+2}{3} \right)^2 S_{ED} + n^2 S_{MD} \right] \tag{3}$$

where J is the total angular momentum of the upper state. Notice that this equation contains a term S_{MD}, the magnetic dipole (MD) line strength. MD transition probabilities can be calculated separately [17,18]. While MD transitions are normally orders of magnitude smaller than ED transitions, because ED transitions for lanthanides in solids occur as a result of a perturbation, some MD transitions will make significant contributions. The MD transition probabilities have been calculated here also and included in table 2. This calculation is discussed in detail in the appendix.

The Judd-Ofelt parameters found in this study are compared to those found in the literature for various germanate glass compositions in table 2. It should be pointed out that caution must be exercised in comparing intensity parameters found in the literature because some older articles use the τ_λ parameter instead of the Ω_λ parameter commonly used today. These forms of the intensity parameter are related by

$$\Omega_\lambda = \frac{3h}{8\pi^2 mc} n \left(\frac{3}{n^2+2} \right)^2 \tau_\lambda \tag{2}$$

where n is the index of refraction and $3h/8\pi^2 mc = 9.2253\text{x}10^{-12}$ cm. Many of the articles by Reisfeld in the 1970's use the τ_λ parameter and should be converted to Ω_λ parameters for proper comparison with modern articles. Comparison of parameters in the literature with the parameters found here are in fair agreement for the most part, with a few exceptions. Discrepancies can arise for a number of reasons since the Judd-Ofelt parameters can be sensitive to the accuracy of the absorption measurements as well as the transitions used in the fit.

Table 2. Comparison of Judd-Ofelt parameters for various germanate glasses.

Glass composition	Ω_2 (x10^{-20} cm^2)	Ω_4 (x10^{-20} cm^2)	Ω_6 (x10^{-20} cm^2)	Reference
GeO_2-PbO	2.81	0.29	0.86	12
GeO_2-PbO-Nb_2O_5	5.55	2.03	1.26	13
GeO_2-BaO-K_2O	3.53	1.38	0.71	4
GeO_2-BaO-K_2O	4.0	1.6	0.8	6
Germanate	6.7	1.04	0.53	7
GeO_2-BaO/CaO-Na_2O/Li_2O	6.14 ± 0.11	1.54 ± 0.02	0.87 ± 0.07	This study

The results of the Judd-Ofelt analysis are shown in table 3. Five absorption measurements were used in the fit to obtain the Judd-Ofelt parameters. The manifolds used in the fit include: $^1D_2$, $^1G_4$, $^3F_2 + {}^3F_3$, $^3H_4$, and $^3F_4$, with the $^3H_5$ excluded.

Table 3. Calculated line strengths, transition probabilities, and branching ratios in Tm:germanate.

TRANSITION	WAVELENGTH (nm)	S_{ED} (x10^{-20} cm^2)	A_{MD} (s^{-1})	A_{ED} (s^{-1})	ß	LIFETIME (ms)
$^3P_0 \rightarrow {}^1I_6$	13550.1	0.020		0.02	0.000	
$^3P_0 \rightarrow {}^1D_2$	1300.2	0.171		231.06	0.002	
$^3P_0 \rightarrow {}^1G_4$	700.9	0.079		696.97	0.006	
$^3P_0 \rightarrow {}^3F_2$	490.4	1.844		49166.96	0.450	
$^3P_0 \rightarrow {}^3F_3$	478.9	0.000		0.00	0.000	
$^3P_0 \rightarrow {}^3H_4$	437.3	0.030		1159.96	0.011	
$^3P_0 \rightarrow {}^3H_5$	368.3	0.000		0.00	0.000	
$^3P_0 \rightarrow {}^3F_4$	336.9	0.426		41228.31	0.377	
$^3P_0 \rightarrow {}^3H_6$	284.6	0.066		16772.62	0.154	0.009
$^1I_6 \rightarrow {}^1D_2$	1438.2	0.000		0.00	0.000	
$^1I_6 \rightarrow {}^1G_4$	739.2	3.642		2096.09	0.113	
$^1I_6 \rightarrow {}^3F_2$	508.8	0.371		677.91	0.036	
$^1I_6 \rightarrow {}^3F_3$	496.5	0.012		22.91	0.001	
$^1I_6 \rightarrow {}^3H_4$	451.9	1.062		2829.27	0.152	
$^1I_6 \rightarrow {}^3H_5$	378.6	0.015	11.11	71.61	0.004	
$^1I_6 \rightarrow {}^3F_4$	345.5	1.561		10526.74	0.565	
$^1I_6 \rightarrow {}^3H_6$	290.7	0.149	87.42	2401.64	0.129	0.053
$^1D_2 \rightarrow {}^1G_4$	1520.7	1.397		235.80	0.006	
$^1D_2 \rightarrow {}^3F_2$	787.4	0.872	45.32	1075.75	0.027	
$^1D_2 \rightarrow {}^3F_3$	758.2	1.122	73.83	1554.21	0.039	
$^1D_2 \rightarrow {}^3H_4$	658.9	1.000		2126.48	0.054	
$^1D_2 \rightarrow {}^3H_5$	513.9	0.017		77.53	0.002	
$^1D_2 \rightarrow {}^3F_4$	454.7	3.879		26346.59	0.666	
$^1D_2 \rightarrow {}^3H_6$	364.3	0.568		8161.99	0.206	0.025
$^1G_4 \rightarrow {}^3F_2$	1632.9	0.186		14.07	0.006	
$^1G_4 \rightarrow {}^3F_3$	1512.2	0.434	2.58	41.36	0.017	

$^1G_4 \rightarrow {}^3H_4$	1162.8	1.289	26.99	271.33	0.109	
$^1G_4 \rightarrow {}^3H_5$	776.2	0.923	112.59	660.86	0.266	
$^1G_4 \rightarrow {}^3F_4$	648.6	0.115	7.07	142.39	0.057	
$^1G_4 \rightarrow {}^3H_6$	479.1	0.423		1349.90	0.544	0.380
$^3F_2 \rightarrow {}^3F_3$	20449.9	0.138	0.01	0.01	0.000	
$^3F_2 \rightarrow {}^3H_4$	4038.8	2.287		20.52	0.013	
$^3F_2 \rightarrow {}^3H_5$	1479.3	0.963		176.59	0.112	
$^3F_2 \rightarrow {}^3F_4$	1076.0	1.967		942.33	0.597	
$^3F_2 \rightarrow {}^3H_6$	678.1	0.225		438.75	0.278	0.634
$^3F_3 \rightarrow {}^3H_4$	5032.7	1.299	0.27	4.30	0.002	
$^3F_3 \rightarrow {}^3H_5$	1594.6	4.396		459.43	0.224	
$^3F_3 \rightarrow {}^3F_4$	1135.7	0.162	49.17	47.05	0.023	
$^3F_3 \rightarrow {}^3H_6$	701.4	1.230		1543.59	0.751	0.475
$^3H_4 \rightarrow {}^3H_5$	2334.3	0.827	6.47	21.39	0.015	
$^3H_4 \rightarrow {}^3F_4$	1466.7	1.175	16.81	122.82	0.084	
$^3H_4 \rightarrow {}^3H_6$	814.9	2.145		1324.99	0.902	0.670
$^3H_5 \rightarrow {}^3F_4$	3946.3	1.568	0.15	6.86	0.031	
$^3H_5 \rightarrow {}^3H_6$	1252.0	1.574	59.19	216.93	0.969	3.531
$^3F_4 \rightarrow {}^3H_6$	1833.9	4.631		247.22	1.000	4.045

The equations governing the rate of change of the populations of the $^3F_4$ and $^3H_4$ manifolds can be written as

$$\frac{dn_2}{dt} = -\frac{n_2}{\tau_2} + 2p_{41}n_1n_4 - 2p_{22}n_2^2 \tag{3}$$

$$\frac{dn_4}{dt} = -\frac{n_4}{\tau_4} - p_{41}n_1n_4 + p_{22}n_2^2 \tag{4}$$

Referring to figure 2, the $^3H_6$, $^3F_4$ and $^3H_4$ manifolds are designated by the numbers 1, 2 and 4, respectively. The energy transfer parameters in the above two equations are illustrated in this figure as well. The p_{41} parameter is the self-quenching process and p_{22} is its reverse process. Although it is not always taken into account, all energy transfer processes can have a forward and reverse process. In the case under consideration here, pumping the $^3F_4$ manifold, the p_{22} is the forward upconversion process and the p_{41} is the reverse self-quenching process.

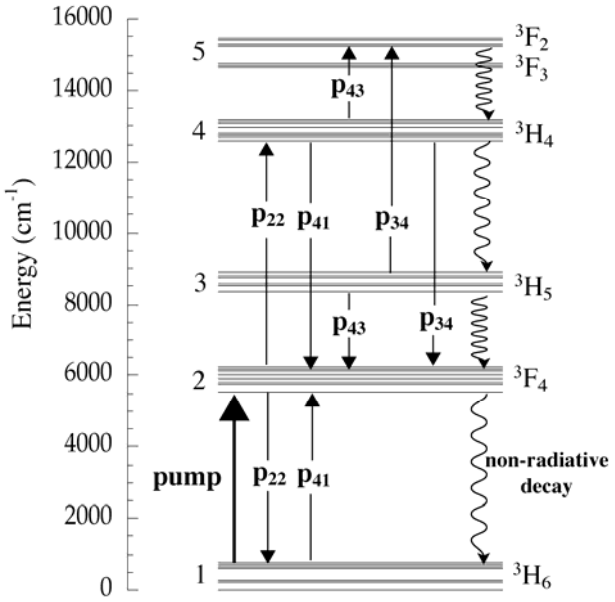

Figure 2. Schematic of Tm-Tm energy transfer processes.

Since there must be conservation of Tm excitations, then $C_{Tm}N_s = n_1 + n_2 + n_4$. This can be used to eliminate n_1 from the equations. In addition, since the majority of excitations reside in the $^3F_4$ pumping level, then $n_2 >> n_4$, and all terms involving the terms n_4^2 and n_2n_4 can be neglected compared to n_2^2 and n_4. This allows equations 3 and 4 to be written as

$$\frac{dn_2}{dt} = -\frac{n_2}{\tau_2} - 2p_{22}n_2^2 \tag{5}$$

$$\frac{dn_4}{dt} = -\left(\frac{1}{\tau_4} + p_{41}C_{Tm}N_s\right)n_4 + p_{22}n_2^2 \tag{6}$$

where C_{Tm} is the percent thulium concentration and N_s is the total density of sites available for occupation by the Tm ions. Eq. 5 can be directly solved and the solution is

$$n_2(t) = \frac{n_{20}\exp(-t/\tau_2)}{1 + 2n_{20}\tau_2 p_{22}\left[1 - \exp(-t/\tau_2)\right]} \tag{7}$$

where n_{20} represents the initial population density for t = 0 at the initiation of the pulse. Eq. 6 is more problematic to solve because the form of Eq. 7 does not lend itself to allowing this equation to be solved in closed form. However, Eq. 7 does not actually deviate substantially from a single exponential. The term in the denominator aids in taking into account the early time behavior of the decay when upconversion takes place. It is a very reasonable approximation to use only the numerator in Eq. 7 to solve Eq 6. With this approximation, equation 6 becomes

$$\frac{dn_4}{dt} = -\left(\tau_4^{-1} + p_{41}C_{Tm}N_s\right)n_4 + p_{22}n_{20}^2 \exp(-2t/\tau_2) \tag{8}$$

Making the substitutions $1/\tau_a = 1/\tau_4 + p_{41}C_{Tm}N_s$ and $1/\tau_b = 2/\tau_2$, a trial solution of the following form can be made

$$n_4(t) = A\exp(-t/\tau_a) + B\exp(-t/\tau_b) \tag{9}$$

At t = 0, $n_4(t) = 0$ and it follows that A = -B. The experimental decay measurements of the $^3H_4 \rightarrow {}^3H_6$ emission and the $^3F_4 \rightarrow {}^3H_6$ emission have been discussed in the experimental method section. The data for the $^3F_4$ decay was fit to Eq. 7 and the data for the $^3H_4$ decay was fit to Eq. 9. The decay profiles are shown in figures 3 and 4 along with the best fit to the data and a single exponential fit for comparison. The fit in figure 4 is so good, in fact, that it is hard to discern from the actual decay curve.

The best fitting parameters from this analysis are shown in tables 4 and 5. The measured lifetime of 4293 μs in the 0.02 Tm_2O_3 sample agrees well with the Judd-Ofelt value of 4045 μs, indicating that nonradiative quenching is not active for this sample. There is clearly a shortening of the $^3F_4$ lifetime with higher concentration. This could be due to some energy transfer among the Tm ions or perhaps the presence of some impurity. Further investigations with a variety of samples containing a range of concentrations would be required to resolve this issue. This lifetime quenching of the Tm $^3F_4$ manifold has been noticed in other Tm crystal and glass materials, but the mechanism has not been clearly understood yet.

Now, regarding the $^3H_4$ lifetimes, recall that $\tau_2 = 2\,\tau_b$ by definition. This was an outcome of solving Eq. 6 for the $^3H_4$ dynamics by assuming the $^3F_4$ decay was predominantly exponential. Figure 3 shows this to be approximately true. From the analysis here, referring to tables 4 and 5, we find that $\tau_2 \cong 2.6\,\tau_b$ in reasonable agreement with the approximation.

Table 4. Fitting parameters of Tm:germanate $^3F_4 \rightarrow {}^3H_6$ lifetime under $^3F_4$ pumping.

Sample	n_{20}	τ_2 (μs)	$n_{20}\tau_2 p_{22}$	R
0.02 Tm_2O_3	0.9204	4293	0.1016	0.9996
0.04 Tm_2O_3	0.9743	2190	0.1092	0.9996

Table 5. Fitting parameters of Tm:germanate $^3H_4 \rightarrow {}^3H_6$ lifetime under $^3F_4$ pumping.

Sample	A	τ_a (μs)	B	τ_b (μs)	R
0.02 Tm_2O_3	-1.149	21.04	1.068	1665	0.9998
0.04 Tm_2O_3	-1.140	10.93	1.028	862	0.9996

The $^3H_4$ luminescence of the 0.02 and 0.04 Tm_2O_3 germanate samples under $^3F_4$ pumping show a very sharp rise time followed by a much longer decay time. Luminescence was also detected from the $^3F_2$, $^3F_3$ manifolds around 0.67 μm with similar time constants. These decay times, τ_b, are longer than what would be expected from the $^3H_4$ or $^3F_2$, $^3F_3$ manifolds. The decay times must reflect the population change of the $^3F_4$ manifold, which feeds the $^3H_4$ through some upconversion process. The rise times reflect the timescale of the energy transfer processes.

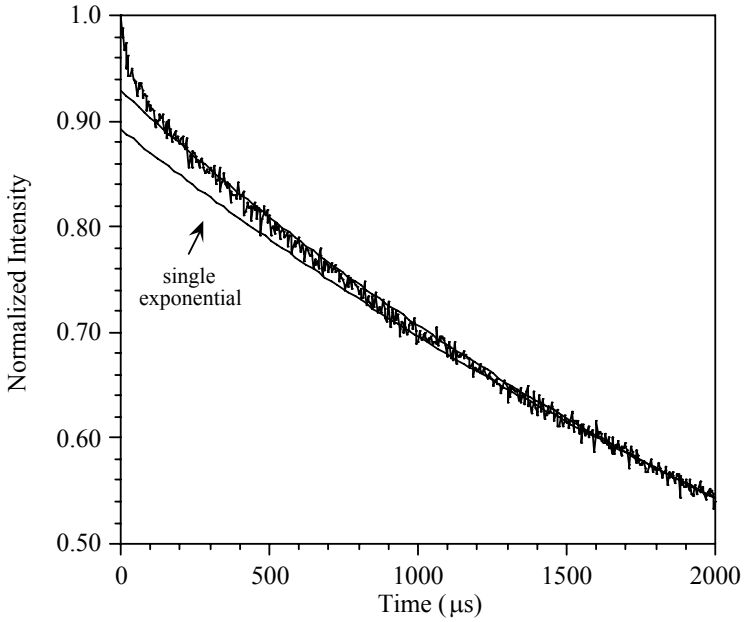

Figure 3. Tm $^3F_4 \rightarrow {}^3H_6$ decay of 2% wt Tm:germanate glass.

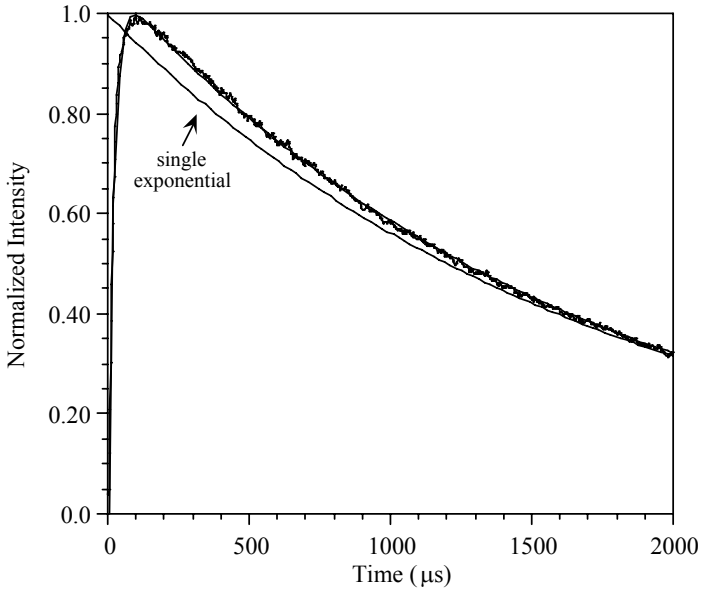

Figure 4. Tm $^3H_4 \rightarrow {}^3H_6$ decay profile of 2% wt Tm:germanate glass.

Figure 2 shows a schematic of a possible scenario regarding the energy transfer processes populating the $^3H_4$ and the $^3F_2$, $^3F_3$ manifolds under $^3F_4$ pumping. These processes are p_{22} (Tm $^3F_4 \rightarrow {}^3H_4$;Tm $^3F_4 \rightarrow {}^3H_6$), p_{43} (Tm $^3H_5 \rightarrow {}^3F_4$;Tm $^3H_4 \rightarrow {}^3F_{2,3}$), and p_{34} (Tm $^3H_4 \rightarrow {}^3F_4$;Tm $^3H_5 \rightarrow {}^3F_{2,3}$). All of the processes also have reverse processes, but only the reverse of p_{22}, designated by p_{41}, is shown. The latter two processes, p_{43} and p_{34} were chosen because they are the most resonant and, therefore, the most likely. For simplicity, the manifolds have been labeled from one to five, with the $^3F_2$ and $^3F_3$ being considered as a single manifold. To get some idea of the relative importance of these processes, the energy transfer rate constants can be written as [19]

$$\frac{p_{ik}}{p_{jl}} = \frac{Z_j Z_l e^{-\Delta E_i/kT} e^{-\Delta E_k/kT}}{Z_i Z_k e^{-\Delta E_j/kT} e^{-\Delta E_l/kT}} \tag{10}$$

The ratio of the forward to reverse process can be calculated from Eq. 10 based only on Boltzmann statistics. It is found that $p_{43}/p_{52} = p_{34}/p_{52} = 1.0565$ and $p_{22}/p_{41} = 0.0038$. This seems to indicate that once p_{22} populates the $^3H_4$ manifold, the dominant process would be p_{41}, and the system self-quenches strongly, but the $^3F_2$, $^3F_3$ manifolds do get populated as is evidenced by the luminescence observed under $^3F_4$ pumping. A curious aspect in considering these issues is that the Tm $^3H_5$ manifold shows no detectable luminescence, even though reciprocity on absorption cross section measurements indicates that is has a respectable emission cross section. It is very likely that a combination of non-radiative and energy transfer processes deplete this manifold very rapidly to levels that cannot be measured. Nevertheless, it is clear that more studies will have to be done to resolve these issues.

The emission cross-section measurements of the $^3F_4 \rightarrow {}^3H_6$ transition have been discussed in the experimental method section. The expression for the cross section is given by

$$\sigma(\lambda) = \frac{\lambda^5}{8\pi c n^2 (\tau_r/\beta)} \frac{3I(\lambda)}{\int \lambda I(\lambda) d\lambda} \tag{11}$$

where $I(\lambda)$ is the emission spectrum intensity, τ_r is the radiative lifetime, β is the branching ratio, or fraction of total photon flux from the upper to lower state, and n is the index of refraction. β=1 for the $^3F_4 \rightarrow {}^3H_6$ transition and $n \cong 1.65$. Since the measured lifetime agrees well with the value determined from the Judd-Ofelt analysis, then non-radiative quenching is absent in Tm:germanate. A value of $\tau_r \cong 4$ ms, as determined by the Judd-Ofelt analysis, was used in Eq. 11 to normalize the emission cross-section. The emission cross section spectrum of Tm:germanate glass is shown in Figure 5.

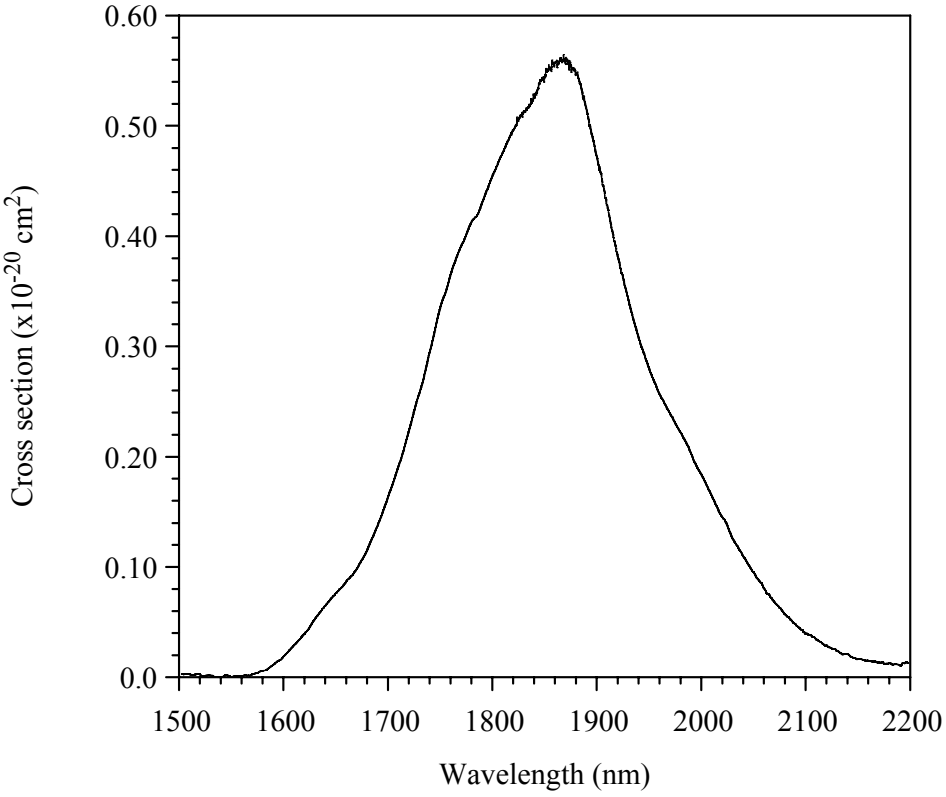

Figure 5. Emission cross section of Tm $^3F_4 \rightarrow {}^3H_6$ transition in Tm:germanate glass.

This spectrum shows the broad features typical of glasses. The peak cross section occurs around 1.865 μm with a value of 5.65x10^{-21} cm^2. Measurements in lead germanate glass have reported this peak emission cross section as 4.2 x10^{-21} cm^2 by Sheperd [9] and as 7.7 x10^{-21} cm^2 by Balda [13]. A study by Zou [11] reports it as 6.8 x10^{-21} cm^2 in alkali germanate glass. Our measurement is certainly within the range of the others. Such values are typical of the relatively small cross sections associated with Tm ions in solids. Although the spectrum is broad as is typical in glasses, it is possible to obtain some information on the energy levels by using the reciprocity of emission and absorption [20, 21]. The emission and absorption cross sections are related by

$$\sigma_{em}(\lambda) = \sigma_{abs}(\lambda)\frac{Z_l}{Z_u}\exp\left[\frac{E_{ZL} - hc/\lambda}{kT}\right] \qquad (6)$$

where Z_l / Z_u is the ratio of partition functions of the lower and upper manifolds, respectively, E_{ZL} is the zero-line, defined as the energy difference between the lowest Stark level of the upper manifold and the lowest Stark level of the lower manifold. The constants are hc = 1x10^7 nm-cm^{-1}, and kT = 0.695 cm^{-1} at room temperature. Generally speaking, the room temperature value of the Z_l / Z_u ratio is typically in the range of 1.2 to 1.6 for most Tm-doped crystals. Performing a reciprocity calculation gives a range for

E_{ZL} of between 5625 and 5685 cm^{-1}, corresponding to between approximately 1759 and 1777 nm. The true value of Z_l / Z_u is not known, but an estimate of the position of the zero-line is likely somewhere in this 18 nm range. This establishes an approximate position of the lowest Stark level of the Tm $^3F_4$ manifold in germanate glass.

3.2 Pulsed laser experiments

The laser measurements have been discussed in the experimental set-up section. Laser output energy versus optical diode pump energy for 7 fiber lengths were fit to a linear relation, defining the threshold and slope efficiency. The laser output energy versus pump energy for the 0.57 and 1.07 m fiber lengths are shown in Figure 6. The slope efficiency and threshold for the 0.57 m fiber was measured to be 12.4% and 32.8 mJ, respectively. For the 1.07 m fiber, 14.0% and 36 mJ were measured. Laser wavelengths ranged between 1.95 and 1.97 μm for the various fiber lengths. Transmitted pump energy versus optical diode pump energy were also recorded versus fiber length. Transmitted pump energy versus fiber length for seven different fiber lengths appears in Figure 7. The fit to this data shows an exponential trend.

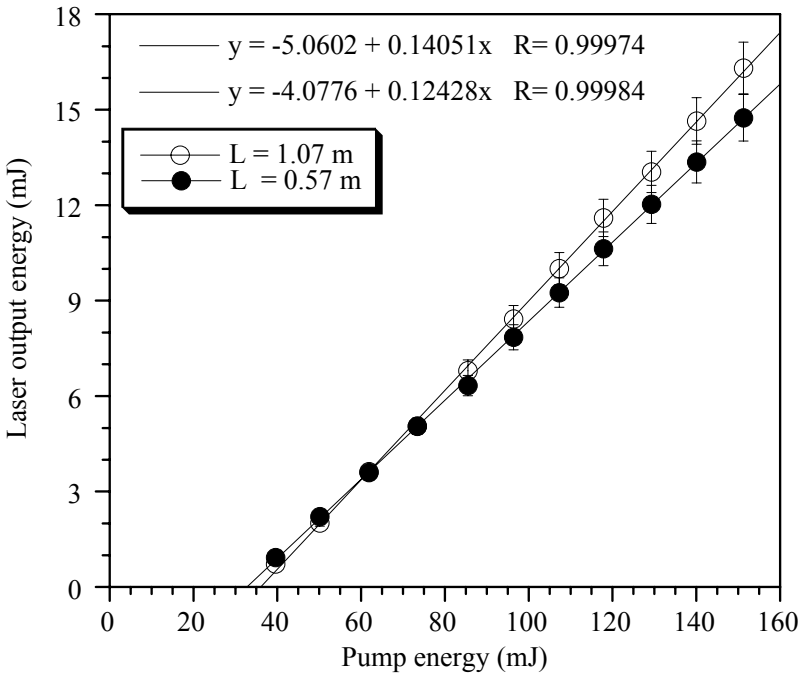

Figure 6. Laser output energy versus pump energy.

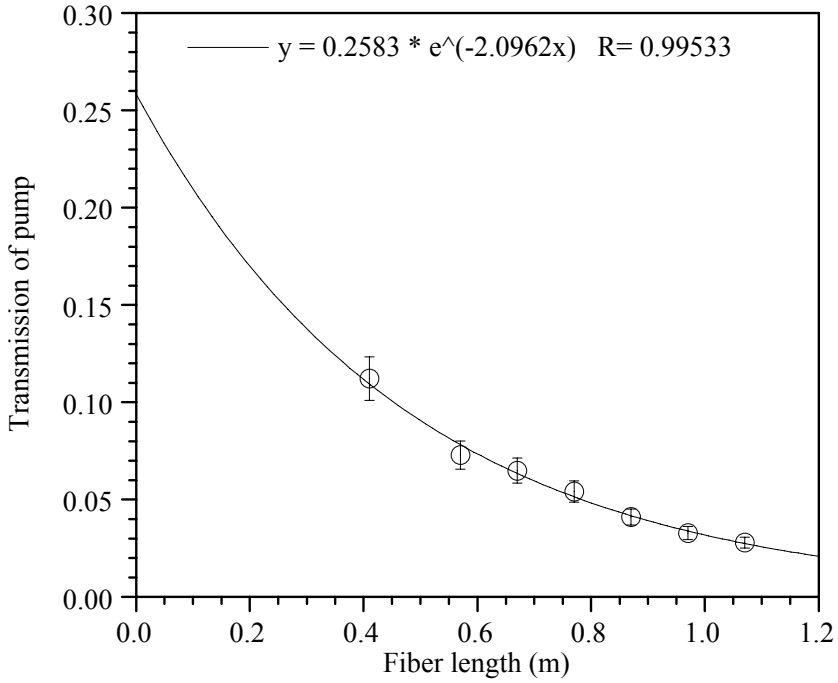

Figure 7. Transmission of pump energy versus Tm:germanate fiber length.

Slope efficiency and transmitted pump energy data were used to infer a quantum efficiency of 1.69. Fitting the transmitted pump energy versus fiber length data to an exponential yields the launch efficiency, η_L, and the average absorption cross-section of the pump radiation, σ_{abs}. The slope efficiency, σ_S, can be approximated by

$$\sigma_s = \frac{\eta_Q \eta_L \lambda_P}{\lambda_L} \left(\frac{1 - R_M}{(1 - R_M) + (1 - R_L)(R_M R_L)^{1/2}} \right) \left(1 - e^{-\sigma_{abs} C_{Tm} N_0 L}\right) \tag{7}$$

where R_M is the output mirror reflectivity, R_L represents the losses, η_Q is the quantum efficiency, L is the fiber length. R_M can be calculated from the Fresnel coefficient because the refractive index is known and R_L can be estimated. Because R_M is so low, the slope efficiency is nearly independent of R_L. Lower values of R_L than the estimated value, 0.95, imply higher values for η_Q. Inserting the measured slope efficiency and measured values for the other parameters on the right hand side yields a quantum efficiency of 1.69.

Discussion

A substantial number of results have been presented here on the spectroscopy and pulsed laser action of Tm:germanate glass. The absorption cross section measurement shown in figure 1 is quite consistent with results in the literature [8, 13]. A Judd-Ofelt analysis relies on accurate absorption measurements. In particular, the integrated absorption cross section over the wavelength range of as many manifolds possible. This

is especially true in the case of Tm ions since there are few manifolds available for study. The integrated absorption cross sections over wavelength for six manifolds was shown in table 1. Due to overlap of the $^3F_2$ and $^3F_3$ manifolds, these manifolds must be treated as a single manifold and the sum of their matrix elements are used in the Judd-Ofelt theory. In practice, the Judd-Ofelt theory has been used with great success to determine branching rations and lifetimes in a great number of ion-host systems. The set of phenomenological parameters, $\Omega_\lambda(\lambda = 2, 4, 6)$, determined by fitting the experimental absorption, in a least squares difference sum, with the Judd-Ofelt expression are shown in table 2 and are compared with the parameters obtained in five other studies [4, 6, 7, 12, 13]. Overall, the Judd-Ofelt parameters shown in table 2 for Tm:germanate glasses show the trend $\Omega_2 > \Omega_4 > \Omega_6$. The exception seems to be the study by Wachtler [12], where the Ω_4 is unusually low. The most likely reason for this is a poor fit to the experimental absorption data. This might explain why Ω_2 is also somewhat lower than might be expected. This could occur if the $^3H_5$ manifold was used in the fit. In Tm-doped materials the $^3H_5$ manifold should not be used in the fit since it has a rather large magnetic dipole component and including it can skew the results. The parameters obtained in this study predicted a Judd-Ofelt radiative lifetime of 4.045 ms, which agrees quite well with the value of 4.293 ms measured for a 0.02 Tm germanate glass sample. This is an indication that nonradiative quenching of the $^3F_4$ laser manifold is not a problem. The quenching of the $^3F_4$ lifetime at 0.04 Tm remains unknown. Further study is needed to resolve this issue.

The emission properties have been measured for the $^3F_4$ cross section and the lifetime dynamics of this manifold. The peak emission cross section measured in this study was in fair agreement with previous studies [9, 11, 13]. In general, cross section measurements are only accurate to approximately 20%. The literature values range from 4.2 to 7.7×10^{-21} cm^2, while this study measured 5.65×10^{-21} cm^2, which is about 25% different from the minimum and maximum values in the literature. An analysis of the emission decay dynamics of the various Tm manifolds yields insight into the optimum laser design. Tm dynamics were studied by pumping the first excited manifold of Tm using a Q-switched Co:MgF_2 laser. Under short pulse pumping the fluorescence decay data, averaged over 1024 fluorescence curves, from the $^3H_4$ and $^3F_4$ manifolds were fit to equations derived from a rate equation model developed in this paper. Data was analyzed for two Tm concentrations, 0.02 and 0.04. Several items are noteworthy. First, the decay curves suggested by the solution of the differential equation for the $^3F_4$ and $^3H_4$ fluorescence provide an excellent fit to the data, with correlation coefficients near one. Second, the approximation of a single exponential in the differential equation for the $^3H_4$ fluorescence is a reasonable approximation. Third, the observed decay constant, τ_b, is indeed nearly half that of τ_2, as expected by the analysis. Fourth, the lifetime τ_2 is reduced in going from 0.02 to 0.04 Tm implying that the lifetime of the Tm $^3F_4$ manifold is quenched at higher concentration. These results have served to elucidate the energy transfer dynamics further.

A diode pumped Tm:germanate fiber laser was constructed and evaluated as a function of fiber length. Despite the large numerical aperture of the Tm:germanate fiber and the fast focusing lens, the launch efficiency into the fiber was low. This is ascribed to a large pump spot radius at the focus into the fiber, ~100 μm, compared with the inner cladding radius of the fiber, 52 μm. In addition, the peak emission of the laser diode array occurred at 0.784 μm with a temperature near 29 °C rather than the peak Tm absorption

near 0.792 μm. Temperature tuning above 29 °C was not pursued to avoid stressing the laser diode array even though the absorption at 29 °C was about half the peak absorption. Although optimal pumping conditions were not achieved, in an ~1 m fiber, ~16 mJ was obtained utilizing a 4.5 ms pump pulse length. Clearly, these results can be improved upon, but the present results allow for an assessment of the quantum efficiency, which is shown to be 1.7. The spectroscopic and laser performance data presented here support the inference of this quantum efficiency.

Summary

Pulsed laser experiments demonstrate that Tm:germanate fiber lasers can operate with a quantum efficiency of 1.7. Spectroscopic parameters needed to characterize a Tm:germanate fiber laser, including cross sections and lifetimes were measured and analyzed. A diode pumped, Tm:germanate fiber laser was constructed and evaluated. Both the spectroscopic and fiber laser performance data support the inference of quantum efficiencies near 1.7. This is probable due to low nonradiative quenching of Tm $^3F_4$ luminescence in germanate glass as predicted.

Appendix

The equation for the magnetic dipole (MD) line strength is

$$S_{MD} = \mu_B^2 \left| \left\langle f^n [SL] J \| \mathbf{L}+2\mathbf{S} \| f^n [S'L'] J' \right\rangle \right|^2 \qquad \text{(A1)}$$

where $\mu_B = (\hbar/2mc)$ and the term in brackets is the magnetic dipole matrix element. These values can also be calculated from LS coupled values tabulated in the book by Nielson and Koster [22], remembering that conversion to intermediate coupling must be used [17,18].

It was noted that the Tm $^3H_5$ manifold was excluded from the fit due to the fact that it has a strong magnetic dipole component. The transition probabilities given in Eq. 3 include both electric and magnetic dipole contributions. The calculation of magnetic dipole transition probabilities is more straightforward than the calculation of electric dipole transitions. The transition probability for MD transitions can be written as

$$A_{MD} = \frac{64\pi^4 e^2}{3h(2J+1)\bar{\lambda}^3} n^3 \left(\frac{h}{2mc} \right)^2 \left| \left\langle f^n [SL] J \| \mathbf{L}+2\mathbf{S} \| f^n [S'L'] J' \right\rangle \right|^2 \qquad \text{(A2)}$$

The matrix elements of the MD operator, **L**+2**S**, as well as the 4 f^n intermediate coupled wavefunctions, are required to make this calculation. The matrix elements can be calculated from Eqs. A3 –A5 [17].

$$\left\langle f^n SLJ \left\| \mathbf{L}+2\mathbf{S} \right\| f^n S'L'J \right\rangle = \left[S(S+1)-L(L+1)+3J(J+1) \right] \left[\frac{2J+1}{4J(J+1)} \right]^{1/2} \tag{A3}$$

$$\left\langle f^n SLJ \left\| \mathbf{L}+2\mathbf{S} \right\| f^n S'L'J-1 \right\rangle = \left\{ \left[(S+L+1)^2 - J^2 \right] \left[\frac{J^2-(L-S)^2}{4J} \right] \right\}^{1/2} \tag{A4}$$

$$\left\langle f^n SLJ \left\| \mathbf{L}+2\mathbf{S} \right\| f^n S'L'J+1 \right\rangle = \left\{ \left[(S+L+1)^2 - (J+1)^2 \right] \left[\frac{(J+1)^2-(L-S)^2}{4(J+1)} \right] \right\}^{1/2} \tag{A5}$$

Many 4 f^n intermediate coupled wavefunctions can be found in the literature. The wavefunctions for Tm^{3+} ions in ethyl sulphate were taken from Krupke [23]. Generally speaking, the wavefunctions, like the matrix elements, are independent of the host material since the energy levels of a given lanthanide ion vary only by relatively small amounts (~ several hundred cm^{-1}) from host to host. This is due to the weak perturbation that the crystal field of the host has on the optically active site of the lanthanide ion embedded in the host material. The intermediate coupled wavefunctions are shown here for Tm^{3+} ions in table A1, taken from the article by Krupke.

Table A1. Intermediate coupled wavefunctions for Tm^{3+} ions.

$$\left| \left[{}^3H_6 \right] \right\rangle = 0.9953 \left| {}^3H_6 \right\rangle + 0.0973 \left| {}^1I_6 \right\rangle$$
$$\left| \left[{}^3F_4 \right] \right\rangle = 0.7817 \left| {}^3F_4 \right\rangle - 0.2804 \left| {}^3H_4 \right\rangle + 0.5567 \left| {}^1G_4 \right\rangle$$
$$\left| \left[{}^3H_5 \right] \right\rangle = 1.0000 \left| {}^3H_5 \right\rangle$$
$$\left| \left[{}^3H_4 \right] \right\rangle = 0.7522 \left| {}^3H_4 \right\rangle + 0.5395 \left| {}^3F_4 \right\rangle - 0.3785 \left| {}^1G_4 \right\rangle$$
$$\left| \left[{}^3F_3 \right] \right\rangle = 1.0000 \left| {}^3F_3 \right\rangle$$
$$\left| \left[{}^3F_2 \right] \right\rangle = -0.8738 \left| {}^3F_2 \right\rangle + 0.4654 \left| {}^1D_2 \right\rangle + 0.1408 \left| {}^3P_2 \right\rangle$$
$$\left| \left[{}^1G_4 \right] \right\rangle = 0.7393 \left| {}^1G_4 \right\rangle + 0.5963 \left| {}^3H_4 \right\rangle - 0.3128 \left| {}^3F_4 \right\rangle$$
$$\left| \left[{}^1D_2 \right] \right\rangle = 0.6400 \left| {}^1D_2 \right\rangle + 0.6284 \left| {}^3P_2 \right\rangle + 0.4422 \left| {}^3F_2 \right\rangle$$
$$\left| \left[{}^1I_6 \right] \right\rangle = 0.9953 \left| {}^1I_6 \right\rangle - 0.0973 \left| {}^3H_6 \right\rangle$$
$$\left| \left[{}^3P_0 \right] \right\rangle = 0.9719 \left| {}^3P_0 \right\rangle - 0.2353 \left| {}^1S_0 \right\rangle$$
$$\left| \left[{}^3P_1 \right] \right\rangle = 1.0000 \left| {}^3P_1 \right\rangle$$
$$\left| \left[{}^3P_2 \right] \right\rangle = -0.7650 \left| {}^3P_2 \right\rangle + 0.2023 \left| {}^3F_2 \right\rangle + 0.6114 \left| {}^1D_2 \right\rangle$$
$$\left| \left[{}^1S_0 \right] \right\rangle = 0.9719 \left| {}^1S_0 \right\rangle + 0.2353 \left| {}^3P_0 \right\rangle$$

If we wish to find the magnetic dipole line strength for the ${}^3H_5 \rightarrow {}^3H_6$ transition, for instance, then the matrix element is calculated using the wavefunctions in table A1 and then utilizing Eq. A5. This is shown below.

$$\left\langle \left[{}^3\mathrm{H}_5 \right] \| \mathbf{L}+2\mathbf{S} \| \left[{}^3\mathrm{H}_6 \right] \right\rangle = 0.9953 \left\langle {}^3\mathrm{H}_5 \| \mathbf{L}+2\mathbf{S} \|^3 \mathrm{H}_6 \right\rangle + 0.0973 \left\langle {}^3\mathrm{H}_5 \| \mathbf{L}+2\mathbf{S} \|^1 \mathrm{I}_6 \right\rangle = 3.2393$$

So, $\left| \left\langle \left[{}^3\mathrm{H}_5 \right] \| \mathbf{L}+2\mathbf{S} \| \left[{}^3\mathrm{H}_6 \right] \right\rangle \right|^2 = 10.4931$

Rearranging Eq. A2 and using $\hbar = 6.5826\text{x}10^{-16}$ eV-s, $c = 2.998\text{x}10^{17}$ nm/s, $e^2 / \mathrm{h}c = 1/137$, the fine structure constant, and $mc^2 = 0.511$ MeV, the constant factor is determined to be

$$\frac{64\pi^4 e^2}{3h}\left(\frac{\mathrm{h}}{2mc}\right)^2 = 2.698 \times 10^{10}\,\mathrm{nm}^3 / \mathrm{s}$$

For $J = 5$, $\bar{\lambda} = 1250$ nm, and $n = 1.65$

$$\frac{n^3}{(2J+1)\bar{\lambda}^3} = 2.0909 \times 10^{-10}\,\mathrm{nm}^{-3}$$

Putting these factors together, the result is

$$\mathrm{A_{MD}} = \left(2.698 \times 10^{10}\,\mathrm{nm}^3 / \mathrm{s}\right) \times \left(2.0909 \times 10^{-10}\,\mathrm{nm}^{-3}\right) \times 10.4931 = 59.194\,\mathrm{s}^{-1}$$

This MD value is clearly a substantial contribution to the total transition probability when compared to the ED value from the Judd-Ofelt analysis in table 3. This demonstrates clearly why the $^3H_5$ manifold was excluded from the Judd-Ofelt fit. Adding the MD value calculated here to the ED values for the $^3H_5$ manifold in table 3, the total transition probability becomes A = 282.98 s^{-1}, resulting in a radiative lifetime of 3.53 ms. The other manifolds can have their radiative lifetimes corrected as well by adding MD contributions. Selection rules are $\Delta S = 0$, $\Delta L = 0$ and $\Delta J = \pm 1$, which narrows the number of calculations that must be performed. Note that the $^3F_4$ manifold has no MD transition.

References

1. S.A. Brawer and W.B. White, J. Chem. Phys. 63 (1975) 2421.
2. D.D. Martino, L.F. Santos, A.C. Marques, and R.M. Almeida, J. Non-Cryst. Solids 293-295 (2001) 394.
3. R. Reisfeld and Y. Eckstein, J. Non-Cryst. Solids 12 (1973) 357.
4. R. Reisfeld and Y. Eckstein, J. Chem. Phys. 63, (1975) 4001.
5. R. Reisfeld, L. Boehm, and N. Spector, Chem. Phys. Lett. 49 (1977) 251.
6. R. Reisfeld and C.K. Jorgensen, Handbook on the Physics and Chemistry of Rare Earths, ed. K.A. Gscheneidner Jr. and L. Eyring vol. IX (Elsevier, Amsterdam, 1987) ch. 58
7. M. Eyal, R. Reisfeld, A. Schiller, C. Jacoboni, and C.K. Jorgensen, Chem. Phys. Lett, 140 (1987) 595.

8. J. Wang, J.R. Lincoln, W.S. Brocklesby, R.S. Deol, C.J. Mackechnie, A. Pearson, A.C. Tropper, D.C. Hanna, and D.N. Payne, J. Appl. Phys. 73 (1993) 8066.
9. D. P. Shepherd, D.J.B. Brinck, J. Wang, A.C. Tropper, D.C. Hanna, G. Kakarantzas, P.D. Townsend, Opt. Lett. 19, (1994) 954.
10. J. McDougall and D.B. Hollis, Phys. Chem. Solids 36 (1995) 52.
11. X. Zou and H. Toratani, J. Non-Cryst. Solids 195 (1996) 113.
12. M.Wachtler, A.Speghini, K. Gatterer, H. P. Fritzer, D. Ajo, and M. Bettinelli, J. Am. Ceram. Soc. 81 (1998) 2045.
13. R. Balda, L.M. Lacha, J. Fernandez, J.M. Fernandez-Navarro, Opt. Mat. 27 (2005) 1771.
14. B.M. Walsh, N.P. Barnes, Appl. Phys. B, 78 (2004) 325.
15. B.R. Judd, Phys. Rev. 127 (1962) 750.
16. G.S. Ofelt, J. Chem. Phys. 37 (1962) 511.
17. B.M. Walsh, Advances in Spectroscopy for Lasers and Sensing, ed. B. Di Bartolo and O. Forte (Springer, Netherlands, 2006) 403.
18. B.M. Walsh, N.P. Barnes, and B. Di Bartolo, J. Appl. Phys. 83 (1998) 2772.
19. B.M. Walsh, N.P. Barnes, and B. Di Bartolo, J. Lumin.,75, (1997) 89.
20. D.E. McCumber, Phys. Rev. 136 (1964) A954.
21. S.A. Payne, L.L. Chase, L.K. Smith, W.L. Kway, and W.F. Krupke, IEEE J. Quant. Elec. 28 (1992) 2619.
22. C.W. Nielson and G.F. Koster, Spectroscopic coefficients of the p^n, d^n, and f^n configurations, (The M.I.T. Press, Cambridge, MA, 1963).
23. W.F. Krupke and J.B. Gruber, Phys. Rev. 139 (1965) A2008.

Figures and Tables

Figures:

Tables: